Scintillation-resistant wavefront sensing based on a multi-aperture phase reconstruction (MAPR) technique

Mathieu Aubailly[*a], Mikhail A. Vorontsov[a-c], Jiang Liu[d]
[a]Intelligent Optics Lab., Univ. of Maryland, 2107 TV Building, College Park, MD USA 20740;
[b]School of Engineering, Univ. of Dayton, 300 College Park, Dayton, OH USA 45469;
[c]Optonicus, LLC, 711 E Monument Ave Ste 101, Dayton, OH USA 45402;
[d]Army Research Laboratory, Adelphi, MD USA 20783

ABSTRACT

A scintillation-resistant sensor that allows retrieval of an input optical wave phase using a multi-aperture phase reconstruction (MAPR) technique is introduced and analyzed. The MAPR sensor is based on a low-resolution lenslet array in the classical Shack-Hartmann arrangement and two high-resolution photo-arrays for simultaneous measurements of pupil- and focal-plane intensity distributions which are used for retrieval of wavefront phase in a two stage process: (a) phase reconstruction inside the sensor pupil sub-regions corresponding to lenslet sub-apertures, and (b) recovery of sub-aperture averaged phase components (piston phases). Numerical simulations demonstrate the efficiency of the MAPR technique in conditions of strong intensity scintillations and presence of wavefront branch points.

Keywords: Wavefront sensing, phase reconstruction, atmospheric turbulence, adaptive optics, intensity scintillation

1. INTRODUCTION

Propagation of optical waves through a medium with random refractive index inhomogeneities such as the Earth atmosphere may result in strong spatial and temporal fluctuations of wavefront phase and intensity distributions commonly referred to as phase aberrations and intensity scintillations, respectively[1-3]. For near-vertical atmospheric propagation paths – typical for astronomical and space surveillance imaging applications – the turbulence-induced intensity scintillations are relatively weak (weak-scintillation regime[2]) and their impact on system performance is relatively small and quite often can be neglected. Weak-scintillation conditions significantly simplify sensing and mitigation of the turbulence-induced wavefront phase aberrations using adaptive optics (AO) techniques[4]. It comes with no surprise that operational principles of wavefront sensors used in conventional AO systems such as Shack-Hartmann wavefront sensors (WFS)[4,5], curvature sensors[6,7] or lateral shearing interferometers[8,9] are based on the assumption of weak scintillations. As experiments and analysis show, these conventional wavefront sensors do not perform well in the conditions of optical wave propagation over near-horizontal or slant atmospheric paths, which are commonly characterized by moderate to strong intensity scintillations. This drawback significantly limits utilization of these wavefront sensing and AO techniques for a number of rapidly growing atmospheric optics applications.

In this paper we introduce and analyze the performance of an optical sensing technique referred to as multi-aperture phase reconstruction (MAPR) which is specifically developed for simultaneous high-resolution sensing of optical field wavefront phase $\varphi(\mathbf{r})$ and intensity $I(\mathbf{r})$ distributions under conditions of strong intensity scintillations. Here $\mathbf{r} = \{x, y\}$ designates a coordinate vector in the MAPR sensor pupil plane. Note that since complex amplitude of an optical field $A(\mathbf{r})$ can be represented in the form $A(\mathbf{r}) = |A(\mathbf{r})| \exp\{j\varphi(\mathbf{r})\}$, where $|A(\mathbf{r})| = I^{1/2}(\mathbf{r})$, and both phase $\varphi(\mathbf{r})$ and amplitude $|A(\mathbf{r})|$ functions can be obtained from the MAPR sensor measurements, the sensor described can also be considered as a complex field sensor.

In section 2 we provide a qualitative comparison between the MAPR sensor and the commonly used Shack-Hartmann and phase diversity sensors, and outline both similarities and differences between these wavefront sensing techniques. This section also presents computational steps that are required for phase reconstruction in the MAPR sensor. Section 3 presents results of the MAPR sensor performance analysis obtained through numerical simulations, and section 4 concludes this paper by summarizing the results.

*mathieu@umd.edu; www.iol.umd.edu

High Energy/Average Power Lasers and Intense Beam Applications VII; Atmospheric and Oceanic Propagation of Electromagnetic Waves VI, edited by Steven J. Davis, Michael C. Heaven, J. Thomas Schriempf, Olga Korotkova, Proc. of SPIE Vol. 8238, 82380L · © 2012 SPIE · CCC code: 0277-786X/12/$18 · doi: 10.1117/12.906080

2. MAPR SENSOR OPERATIONAL PRINCIPLE

2.1. MAPR vs. Shack-Hartmann and phase diversity sensors

The notional schematic of the MAPR sensor is shown in Fig. 1(a). The sensor is composed of an optical reducer, a beam splitter, a lenslet array, and pupil- and focal-plane photo-arrays PA_P and PA_F. The optical reducer and beam splitter are used for reimaging of the sensor pupil onto both the photo-arrays PA_P and lenslet array. Photo-array PA_P provides measurements of the input wave intensity distribution $I^P(\mathbf{r}) = I(M\mathbf{r})$ that is scaled by a factor M by the beam reducer. To simplify notations we assume $M = 1$ and $I^P(\mathbf{r}) = I(\mathbf{r})$, and only consider a rectangular lenslet array and photo-arrays respectively composed of $N_l = n_l \times n_l$ lenslets and $N_p = n_p \times n_p$ pixels, where n_l and n_p are integer numbers characterizing lenslet and photo-arrays spatial resolutions. The optical assembly composed of the lenslet array and focal-plane photo-array PA_F in Fig. 1(a) is similar to a conventional Shack-Hartmann (SH) wavefront sensor as shown in Fig. 1(b)[4]. An important difference between these two sensors is that the spatial resolution of the reconstructed phase $\tilde{\varphi}(\mathbf{r})$ for the SH sensor is limited by the resolution of the lenslet array, while the resolution for the corresponding MAPR sensor is determined only by the resolution of photo-arrays. Depending on applications, the number of pixels N_p in a photo-array used in SH sensors usually ranges from $N_p = 128 \times 128$ to $N_p = 512 \times 512$ or sometimes higher, while the number of lenslets N_l seldom exceeds $N_l = 32 \times 32$. In contrast with SH sensors, high-resolution wavefront sensing is achieved in the MAPR sensor using a relatively low-resolution lenslet array. As shown below, the number of lenslets N_l in the MAPR sensor depends on the level of intensity scintillations of the input wave and typically does not exceed $N_l = 4 \times 4$ lenslets even in conditions of strong intensity scintillations.

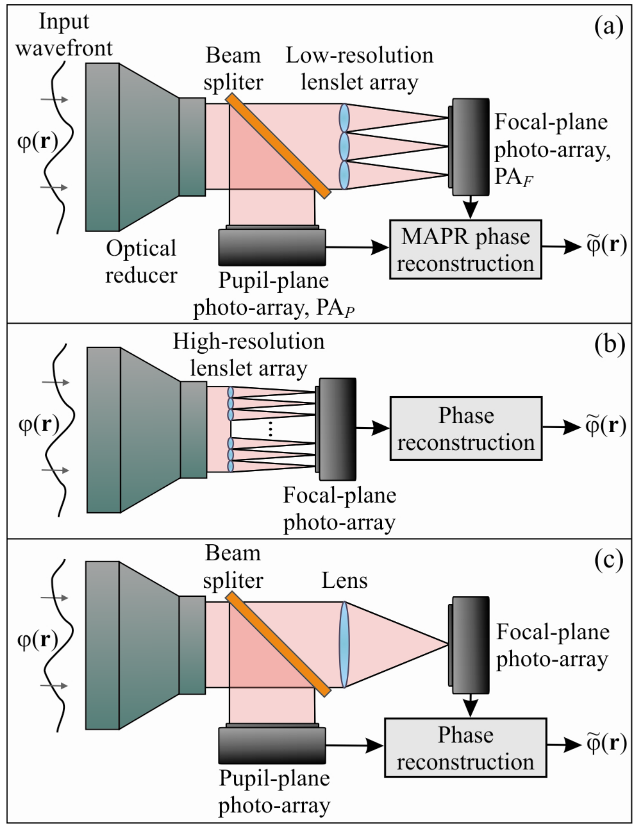

Fig. 1: Notional schematics of (a) MAPR, (b) Shack-Hartmann, and (c) lens analyzer (phase diversity) wavefront sensors.

Another major difference between SH and MAPR sensors is related with the phase reconstruction technique. In SH wavefront sensors phase reconstruction is based on estimating wavefront slopes averaged over lenslet sub-aperture areas $\{\Omega_l\}$. These wavefront slopes, denoted by vectors $\{\mathbf{p}_l\}$ $(l = 1, \ldots, N_l)$, are used for computation of phase functions $\tilde{\varphi}_l(\mathbf{r})$ within the entire SH sensor aperture. Slope vectors $\{\mathbf{p}_l\}$ are obtained by computing displacements of the lenslet focal spots using subsets $\{I_l^F(\mathbf{r})\}$ of the focal-plane intensity distribution $I^F(\mathbf{r})$. Here the function $I_l^F(\mathbf{r})$ is defined within the l^{th} lenslet sub-aperture Ω_l and $\mathbf{r} \in \Omega_l$. The subsets $\{I_l^F(\mathbf{r})\}$ of the focal-plane intensity distribution are also used in the MAPR sensor, not for computation of the wavefront slopes, but rather for retrieval of phase functions $\{\tilde{\varphi}_l(\mathbf{r})\}$ $(l = 1, \ldots, N_l)$ inside the sub-aperture regions $\{\Omega_l\}$. These functions are referred to here as *local* phases. With the exception of unknown constants $\{\Delta_l\}$ (piston phases), these local phases $\{\tilde{\varphi}_l(\mathbf{r})\}$ represent estimates of the true phase $\varphi(\mathbf{r})$ within their corresponding lenslet sub-aperture regions $\{\Omega_l\}$, that is $\varphi_l(\mathbf{r}) \cong \tilde{\varphi}_l(\mathbf{r}) + \Delta_l$, where $\varphi_l(\mathbf{r})$ is the true phase inside Ω_l. The piston phases $\{\Delta_l\}$ are determined during the second stage of the MAPR phase reconstruction algorithm as described in section 2.3.

Computation of local phases $\{\tilde{\varphi}_l(\mathbf{r})\}$ in the MAPR sensor can be achieved using well known iterative algorithms such as the Gerchberg-Saxton[10], phase diversity[11], or conditional gradient descent optimization[12]. Note that these iterative algorithms were originally developed for phase reconstruction in a wavefront sensor commonly referred to as lens analyzer[12] or phase diversity sensor[13]. A notional schematic of this sensor is shown in Fig. 1(c) which includes a single lens, and pupil- and focal-plane photo-arrays. In this sensor, retrieval of the phase function $\varphi(\mathbf{r})$ over the entire sensor aperture is based on iterative processing of the simultaneously captured pupil- and focal-plane intensity distributions, $I^P(\mathbf{r})$ and $I^F(\mathbf{r})$. In contrast, in the MAPR sensor in Fig. 1(a) retrieval of local phases inside the lenslet sub-aperture regions $\{\Omega_l\}$ is performed using corresponding subsets $\{I_l^P(\mathbf{r})\}$ and $\{I_l^F(\mathbf{r})\}$ of the measured intensity distributions $I^P(\mathbf{r})$ and $I^F(\mathbf{r})$ as described in section 2.2.

In general terms, the MAPR wavefront sensing technique integrates both zonal (aperture division) and modal (phase retrieval over entire aperture) approaches that are utilized correspondingly in the Shack-Hartmann and the lens analyzer (phase diversity) wavefront sensors. Similarly to the SH sensor, the input wavefront is sub-divided into an array of equally-sized zones defined by the lenslet sub-apertures. At the same time in each zone high-resolution phase retrieval is based on processing of the corresponding pupil- and focal-plane intensity distributions that are dependent on wavefront phase within the entire sub-aperture — a characteristic of the modal wavefront sensing approach[4]. The final step of phase reconstruction over the entire aperture includes retrieval of piston phases.

Merging both wavefront sensing approaches (zonal and modal) has several advantages. First, note that spatial fluctuations of the input wave intensity and phase inside lenslet sub-aperture areas are less severe than over the entire sensor aperture. For this reason reconstruction of local phase functions in the MAPR sensor most likely results in faster convergence compared to the corresponding reconstruction over the entire aperture as implemented in the lens analyzer sensor. As shown in section 3, this results in a more robust phase reconstruction in conditions of strong intensity scintillations compared to both SH and lens analyzer sensors. Another potential advantage of the MAPR sensor is related with computational efficiency. Reconstruction of local phases in the MAPR sensor can be implemented in parallel, i.e., through simultaneous processing of pupil- and focal-plane intensities subsets as illustrated in Fig. 2. This parallel processing can significantly reduce computational time. Additional increase of the phase reconstruction speed can be achieved with parallel readout of intensity data from the photo-array regions corresponding to lenslet sub-apertures.

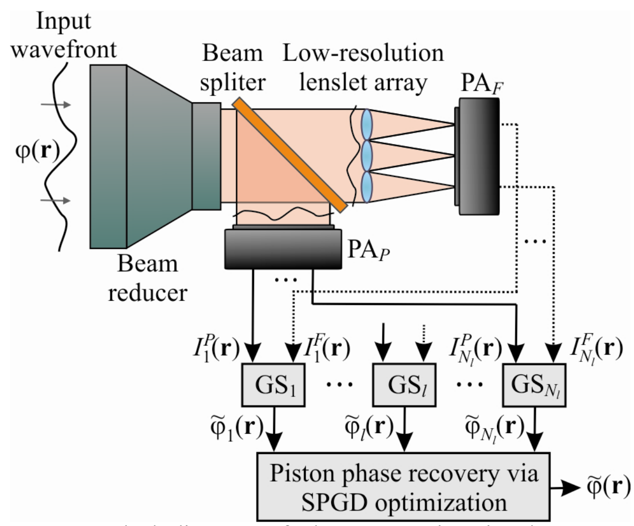

Fig. 2: Block-diagram of data processing in the MAPR wavefront sensor using parallel computation of local phases $\{\tilde{\varphi}_l(\mathbf{r})\}$ with the Gerchberg-Saxton algorithm (computational blocks $\{GS_l\}$) and piston phase reconstruction based on stochastic parallel gradient descent (SPGD) optimization techniques.

As previously mentioned, the aperture size of individual lenses in the lenslet array of MAPR sensor is significantly larger than in the SH sensor. This increase of lenslet aperture size without sacrificing spatial resolution in optical phase reconstruction is highly desirable for sensing of phase aberrations that are composed of both large- and small-scale components. The presence of a large-scale phase aberration component may result in significant displacements of the lenslet focal spots. In the case of a conventional SH sensor with relatively small size lenslets, this may result in focal spot displacements outside the photo-array regions corresponding to lenslet sub-apertures causing optical coupling (crosstalk) between neighboring photo-array regions, inaccurate estimation of centroid displacements and subsequent errors in phase measurements. The use of larger size lenslets in the MAPR sensor allows a significant reduction of such crosstalks.

2.2. Retrieval of local phases

As already mentioned, reconstruction of phase $\varphi(\mathbf{r})$ from measured intensity distributions $I^P(\mathbf{r})$ and $I^F(\mathbf{r})$ in the MAPR sensor is performed in two steps: (1) retrieval of local phases $\{\tilde{\varphi}_l(\mathbf{r})\}$ and (2) recovery of piston (sub-aperture averaged) phases $\{\Delta_l\}$. Several techniques can potentially be applied for computation of local phases from the pupil- and focal-plane subsets, $\{I_l^P(\mathbf{r})\}$ and $\{I_l^F(\mathbf{r})\}$[10-15]. For simplicity we consider here only the Gerchberg-Saxton (GS) algorithm which represents the most known and widely used phase reconstruction method[10].

Consider briefly the GS iterative procedure for reconstruction of local phase $\tilde{\varphi}_l(\mathbf{r})$ at the l^{th} sub-aperture. The phase function $\tilde{\varphi}_l(\mathbf{r})$ is obtain by computing a sequence of the corresponding phase functions $\{\tilde{\varphi}_l(\mathbf{r}, n)\}$, that presumably converges to $\tilde{\varphi}_l(\mathbf{r}) \cong \varphi_l(\mathbf{r}) + const$ after a number of iterations N_{it}. Here $n = 0,1,\dots,N_{it}$ and $\tilde{\varphi}_l(\mathbf{r},0)$ correspond to the iteration index and an arbitrarily chosen initial phase. Convergence of the iterative process is typically evaluated by calculating a measure (metric) $J_l(n) = J[\tilde{\varphi}_l(\mathbf{r},n)]$ that depends on the reconstructed local phase $\tilde{\varphi}_l(\mathbf{r},n)$ at the n^{th} iteration. Computation of phase $\tilde{\varphi}_l(\mathbf{r},n+1)$ at the $(n+1)^{\text{th}}$ GS iteration includes the following steps:

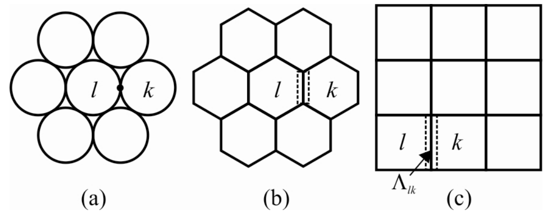

Fig. 3: Examples of densely-packed lenslet array configuration for different lenslet shapes: (a) circular, (b) hexagonal, and (c) rectangular. The dot in (a) and dashed rectangular in (b) and (c) indicate the region (Λ_{lk}) used for piston phase reconstruction.

(a) Computation of the pupil-plane complex function $A_l^P(\mathbf{r},n) = \sqrt{I_l^P(\mathbf{r})}\exp[i\tilde{\varphi}_l(\mathbf{r},n)]$ using the l^{th} subset of the measured pupil-plane intensity $I_l^P(\mathbf{r})$ and local phase $\tilde{\varphi}_l(\mathbf{r},n)$ obtained at the n^{th} iteration;

(b) Computation of the complex field in the focal plane of the l^{th} lenslet $A_l^F(\mathbf{r},n) = Q[A_l^P(\mathbf{r},n)]$, where Q is the operator describing propagation of an optical wave from the lenslet pupil plane to the focal plane. For an ideal lenslet, Q represents the Fourier-transform operator;

(c) Computation of an auxiliary complex function at the lenslet focal plane (focal-plane complex field): $\psi_l^F(\mathbf{r},n) = \sqrt{I_l^F(\mathbf{r})}\exp[i\varphi_l^F(\mathbf{r},n)]$, where $\varphi_l^F(\mathbf{r},n) = arg[A_l^F(\mathbf{r},n)]$ is the phase of the complex field $A_l^F(\mathbf{r},n)$ and $I_l^F(\mathbf{r})$ is the l^{th} subset of the measured focal-plane intensity;

(d) Computation of an auxiliary complex function at the pupil plane (pupil-plane complex field): $\psi_l^P(\mathbf{r},n) = Q^{-\mathbf{1}}[\psi_l^F(\mathbf{r},n)]$, where $Q^{-\mathbf{1}}$ is the inverse operator with respect to Q. This operator describes propagation of the optical wave with complex amplitude $\psi_l^F(\mathbf{r},n)$ from the lenslet focal plane to the pupil plane;

(e) Approximation of the local phase at the $(n+1)^{\text{th}}$ iteration is then given by $\tilde{\varphi}_l(\mathbf{r},n+1) = \arg[\psi_l^P(\mathbf{r},n)]$.

Note that the GS algorithm is equivalent to the conditional gradient descent optimization technique for minimization of the mean-square phase error[12].

The iterative procedure (a) through (e) is repeated a number of iterations N_{it} to ensure convergence of sequence $\{\tilde{\varphi}_l(\mathbf{r},n+1)\}$ toward a small vicinity of the stationary state phase. The number of required iterations N_{it} is commonly defined from the condition $\epsilon(n = N_{it}) = |[J_l(n) - J_l(n-1)]/J_l(n)| \leq \epsilon_0 \ll 1$. The phase function $\tilde{\varphi}_l(\mathbf{r}) \equiv \tilde{\varphi}_l(\mathbf{r},N_{it})$ corresponding to the last iteration is considered as an estimate of $\varphi_l(\mathbf{r})$. Note that due to the existence of local minima of the phase error metric $J_l(n)$ the GS iterative process can in principle converge to different phase functions. The probability of GS process converging to a local minimum increases with the strength of input wave intensity scintillations and phase aberrations. In the strong scintillation regime phase function $\varphi(\mathbf{r})$ can contain phase singularities in the form of branch points[16,17] whose presence significantly reduces convergence speed and most likely results in convergence to a local minimum.

2.3. Computation of piston phases

Consider now the algorithm for retrieval of the piston (sub-aperture-averaged) phases $\{\Delta_l\}$. The general idea is based on the assumption that the lens array is composed of densely packed lenslets, and the local phase functions $\{\tilde{\varphi}_l(\mathbf{r})\}$ in boundary regions between adjacent sub-apertures are alike.

This assumption can be formulated as a continuity requirement for the true phase function $\varphi(\mathbf{r})$ and its first and second derivatives at the boundary regions between adjacent lenslets. To illustrate, consider three geometries of a densely-packed lenslet array shown in Fig. 3. In the case of lenslets with a circular aperture as shown in Fig. 3(a), the boundary between two adjacent lenslets is reduced to a single point, while in the case of hexagonal and rectangular lenslet shapes as in Figs. 3(b) and 3(c) the corresponding boundary is a line segment. The last two lenslet array geometries are advantageous since they allow estimation of piston phases based on phase continuity over line segments belonging to adjacent sub-apertures rather than continuity at a limited number of adjacent points as in Fig. 3(a). This results in significant improvement of accuracy in piston phase retrieval. In the numerical simulations described in section 3 we consider MAPR sensors with rectangular lenslet array geometry.

In the lenslet array in Fig. 3(b) or 3(c) consider a set of points $\{\mathbf{r}_{lk}^{b}\}$ belonging to the boundary line segment Λ_{lk} separating the l^{th} sub-aperture from the adjacent k^{th} sub-aperture as shown in Fig. 3(c), and introduce the corresponding boundary window function $\rho_{lk}(\mathbf{r}-\mathbf{r}_{lk}^{b}) = \exp\left[-\left|\mathbf{r}-\mathbf{r}_{lk}^{b}\right|^2/w^2\right]$ for $\mathbf{r} \in \Omega_l$ and $\rho_{lk}(\mathbf{r}-\mathbf{r}_{lk}^{b}) = 0$ otherwise, where w is the boundary width parameter.

Consider the following function (phase continuity metric) that depends on the piston phases

$$J(\Delta_1, \dots, \Delta_{N_l}) = \sum_{l=1}^{N_l} \left\{ \alpha\epsilon_l^{(0)}(\Delta_1, \dots, \Delta_{N_l}) + \beta\epsilon_l^{(1)}(\Delta_1, \dots, \Delta_{N_l}) + \chi\epsilon_l^{(2)}(\Delta_1, \dots, \Delta_{N_l}) \right\}, \tag{1}$$

where α, β and χ are constant values (weighting coefficients) ranging from zero to one and

$$\epsilon_l^{(m)}(\Delta_1, \dots, \Delta_{N_l}) = \sum_{k \neq l}^{M_l} \left\{ \left[\int_{\Omega_l} \rho_{lk}(\mathbf{r}-\mathbf{r}_{lk}^{b}) Q_m[\tilde{\varphi}_l(\mathbf{r})] d^2\mathbf{r} - \int_{\Omega_k} \rho_{kl}(\mathbf{r}-\mathbf{r}_{lk}^{b}) Q_m[\tilde{\varphi}_k(\mathbf{r})] d^2\mathbf{r} \right]^2 \right\} \tag{2}$$

are measures of the phase continuity between the l^{th} sub-aperture and its M_l neighboring sub-apertures in the lenslet array. Here $m = \{0,1,2\}$, $Q_0[\tilde{\varphi}_l(\mathbf{r})] = \tilde{\varphi}_l(\mathbf{r})$, $Q_1[\tilde{\varphi}_l(\mathbf{r})] = |\nabla\tilde{\varphi}_l(\mathbf{r})|$, and $Q_2[\tilde{\varphi}_l(\mathbf{r})] = |\nabla^2\tilde{\varphi}_l(\mathbf{r})|$. In Eq. (1) the term $\epsilon_l^{(0)}(\Delta_1, \dots, \Delta_{N_l})$ evaluates the squared difference integrated over the boundary area [as defined by the window functions $\{\rho_{lk}(\mathbf{r}-\mathbf{r}_{lk}^{b})\}$] between the local phase $\tilde{\varphi}_l(\mathbf{r})$ and the corresponding local phase values for all neighboring sub-apertures. Similarly, the terms $\epsilon_l^{(1)}(\Delta_1, \dots, \Delta_{N_l})$ and $\epsilon_l^{(2)}(\Delta_1, \dots, \Delta_{N_l})$ are included into the continuity metric [Eq. (1)] for evaluation of averaged difference between boundary values of local phase first and second derivatives represented by gradient $|\nabla\tilde{\varphi}_l(\mathbf{r})|$ and Laplacian $|\nabla^2\tilde{\varphi}_l(\mathbf{r})|$ operators. Note that the width of the boundary window function (parameter w) is chosen based on a priori information about characteristic spatial scale of phase inhomogeneities and noise level.

Computation of piston phases in the MAPR sensor is based on minimization of the phase continuity metric [Eq. (1)] as a function of variables $\{\Delta_l\}$. Metric minimization can be performed using the iterative Stochastic Parallel Gradient Descent (SPGD) technique[18]. In this technique the desired piston phases $\{\Delta_l\}$ are obtained using the following iterative procedure:

$$\Delta_l^{(n+1)} = \Delta_l^{(n)} + \gamma^{(n)}\delta J^{(n)}\delta\Delta_l^{(n)}, l = 1, \dots, N_l, \tag{3}$$

where $\{\Delta_l^{(n)}\}$ are estimates of piston phases at the n^{th} iteration, $\{\delta\Delta_l^{(n)}\}$ and $\delta J^{(n)}$ are correspondingly small-amplitude random perturbations of piston phases and the metric change resulting from these perturbations, and $\gamma^{(n)}$ is a gain coefficient. The iterative process of the piston phase update [Eq. (3)] is repeated until convergence and the resulting stationary state values of piston phases $\{\widetilde{\Delta}_l\}$ are used to compute wavefront phase $\tilde{\varphi}(\mathbf{r})$ over the entire aperture of the MAPR sensor in the form:

$$\tilde{\varphi}(\mathbf{r}) = \sum_{l=1}^{N_l} [\tilde{\varphi}_l(\mathbf{r}) + \widetilde{\Delta}_l]. \tag{4}$$

3. PERFORMANCE ANALYSIS

In this section we present results of the MAPR sensor performance analysis and discuss techniques that can facilitate wavefront reconstruction efficiency.

3.1. MAPR sensor numerical model

In the analysis of the MAPR sensor performance we used an ensemble of computer generated random fields as the sensor's input optical waves. Each realization of the input field complex amplitude $A_{in}(\mathbf{r})$ in the sensor's pupil plane was obtained using the conventional split-operator based wave-optics simulation of optical beam propagation in a volume atmospheric turbulence[19]. At the beginning of the propagation path at $z = 0$ we used a monochromatic, collimated super-Gaussian beam with complex amplitude $A(\mathbf{r}, z = 0) = A_0 \exp\{-[|\mathbf{r}|^2/(2a_0^2)]^8\}$, where A_0 is amplitude, $a_0 = D/2$ is beam width, and D is the MAPR sensor aperture diameter. The optical field complex amplitude at the propagation path end at $z = L$ was utilized as the MAPR sensor input field: $A_{in}(\mathbf{r}) = A(\mathbf{r}, z = L)$. Optical inhomogeneities along the propagation path were modeled with a set of 10 random thin phase screens corresponding to the Kolmogorov turbulence power spectrum[20]. The phase screens were equally spaced along the propagation path and their impact (turbulence strength) was characterized by the ratio D/r_0 where r_0 is a characteristic Fried parameter for plane wave[21]. By varying D/r_0 and propagation distance L one can control strength of input field phase aberrations and intensity scintillations. In the numerical simulations, D/r_0 was ranging from zero (free-space propagation) to 12, and the propagation distance from $L = 0$ (no intensity scintillations) to $L = 0.1L_{dif}$, where $L_{dif} = k(D/2)^2$ is the diffractive distance, and $k = 2\pi/\lambda$ is wave number. Figs. 4(a)-(d) show examples of the input field intensity and phase distributions which are obtained using the technique described above. Note that the phase distributions in Figs. 4(c) and 4(d) contain phase discontinuities (branch points) that can be seen as "forks" in the corresponding interference fringes in Figs. 4(e) and 4(f). The interference patterns $I_{INT}(\mathbf{r})$ in this and other figures are used for qualitative evaluation of the phase reconstruction performance. The interference patterns were computed using the following expression: $I_{INT}(\mathbf{r}) = 1 + \cos\{\arg[A_{in}(\mathbf{r})] + \kappa_0 x\}$, where κ_0 is a constant defining spatial frequency of the interference fringes.

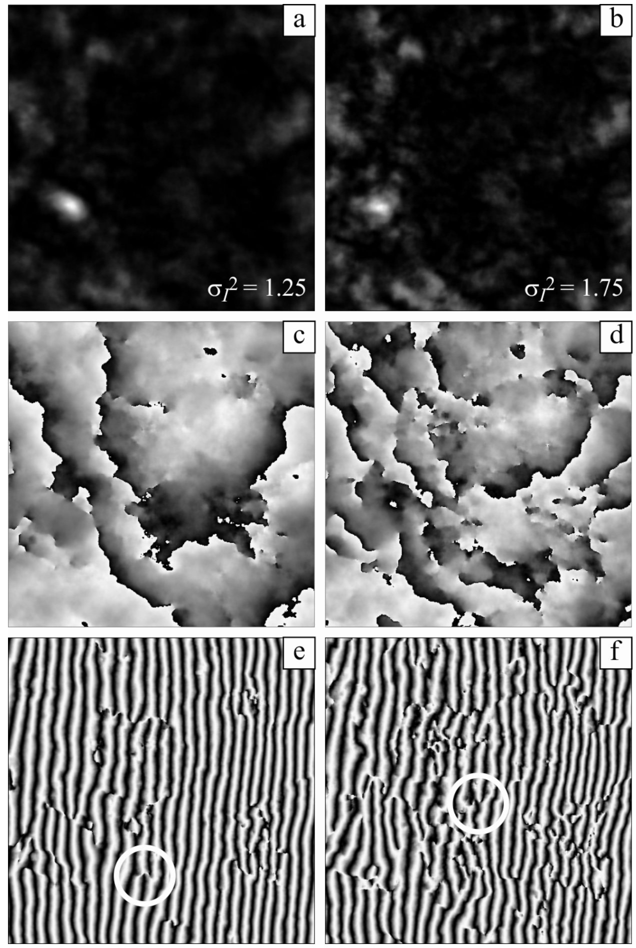

Fig. 4: Grey-scale images corresponding to computer generated optical field intensity (a,b) and phase (c,d) distributions at the MAPR sensor pupil plane for $D/r_0 = 8$ (a,c) and $D/r_0 = 12$ (b,d). Phase distributions in (c,d) are shown inside 2π range [between $-\pi$ (black) and $+\pi$ (white)]. The corresponding phase interference patterns are shown in (e,f). The interference pattern "forks" inside the white circles indicate branch points.

The strength of the input field intensity scintillations was characterized by the aperture-averaged scintillation index

$$\sigma_I^2 = \frac{1}{S}\int \left\{\frac{\langle [I^P(\mathbf{r})]^2\rangle}{\langle I^P(\mathbf{r})\rangle^2} - 1\right\} d^2\mathbf{r}, \qquad (7)$$

where $I^P(\mathbf{r}) = |A_{in}(\mathbf{r})|^2$ and S is the MAPR sensor aperture area. Here $\langle . \rangle$ denotes averaging over ensemble of input fields corresponding to statistically independent realizations of phase screens. In the numerical simulations, 50 sets of phase screens were used for ensemble averaging. Dependence of σ_I^2 on parameter D/r_0 in Fig. 5 shows the range of intensity scintillation used in predictive simulations of the MAPR sensor performance. Change of parameter D/r_0 from zero to $D/r_0 = 12$ allows generation of sensor input fields with a wide range of scintillation index values ($0 \le \sigma_I^2 \le 1.75$).

In the numerical simulations we assumed rectangular lenslet arrays with the number of lenslets in rows and columns ranging from $n_l = 2$ to $n_l = 7$. Each lenslet was represented by a phase mask with parabolic phase profile $\varphi_l(\mathbf{r}) = k|\mathbf{r} - \mathbf{r}_l|^2/(2F)$, where $\mathbf{r} \in \Omega_l$, $\mathbf{r}_l$ is the coordinate vector corresponding to l^{th} lenslet center, and F is the focal distance. Note that in practice individual lenslets are separated by narrow gaps. These gaps were modeled by absorbing masks located along the lenslet edges. The mask width was set to 5% of the lenslet size. Intensity distribution in the lenslet focal plane was calculated by considering input wave propagation through the corresponding combined phase and intensity mask with further diffraction over distance F. Fig. 6 shows examples of the simulated focal-plane intensity distributions for a 3×3 lens array.

3.2. Phase retrieval accuracy evaluation

In the numerical simulations of the MAPR sensor we used Gerchberg-Saxton (GS) algorithm for reconstruction of local phases (see section 2.2) and the SPGD-based continuity metric minimization technique described in section 2.3 for computation of piston phases. Examples of such simulations are illustrated in Fig. 7. The first stage of MAPR computations resulted in reconstruction of local phases, as shown in Fig. 7(a,b). The visible sharp boundaries between lenslet regions in the gray scale images in Fig. 7(a,b) indicate the existence of errors in piston phases. With retrieval of piston phases at the second step of the MAPR computations these boundaries are nearly vanished [see the corresponding images in Fig. 7(c,d)].

The accuracy of phase reconstruction can be evaluated with the use of the interference fringe patterns generated for an optical field with uniform intensity and residual phase $\delta(\mathbf{r}) = \varphi(\mathbf{r}) - \tilde{\varphi}(\mathbf{r})$. Consider first the interference patterns in Fig. 7(e,f) which correspond to reconstructed local phases in Fig. 7(a,b). Undistorted vertical interference fringes within lenslet regions and discontinuity of these fringes along region boundaries indicate both high-quality of local phase reconstruction and presence of significant errors in piston phases. Retrieval of piston phases resulted in continuity of fringes within the entire sensor aperture as seen in Fig. 7(g,h). Note that the piston phases can be reconstructed in parallel with local phases by nesting the SPGD iterative calculations into the Gerchberg-Saxton iterative procedure. This technique of nested GS and SPGD iterative cycles was used in all calculations described.

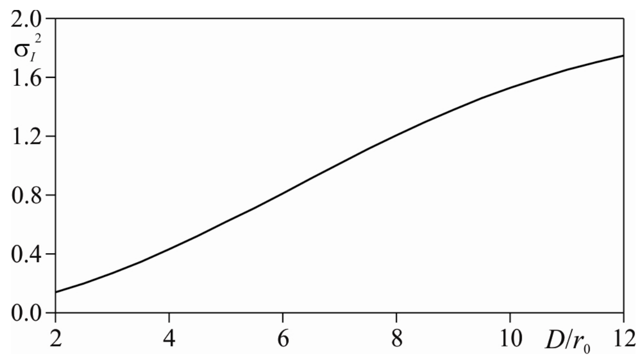

Fig. 5: Aperture-averaged scintillation index for the MAPR sensor input fields used in the numerical simulation vs. D/r_0 for $L = 0.1L_{dif}$.

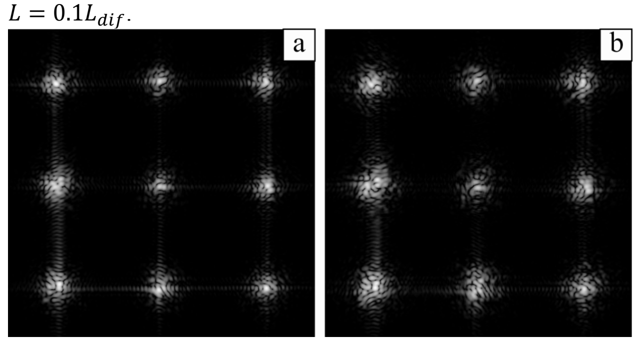

Fig. 6: Intensity distributions in the MAPR sensor lens-let focal plane for input fields shown in Fig. 4: (a) $D/r_0 = 8$ and (b) $D/r_0 = 12$.

Accuracy of phase reconstruction can also be evaluated using the Strehl ratio that is defined here as[22]

$$St(n) = \left|\iint |A_{in}(\mathbf{r})| \exp[i\delta(\mathbf{r},n)]\, d^2\mathbf{r}\right|^2 \Big/ \left[\iint |A_{in}(\mathbf{r})| d^2\mathbf{r}\right]^2, \tag{8}$$

where $\delta(\mathbf{r},n) = \varphi(\mathbf{r}) - \tilde{\varphi}(\mathbf{r},n)$ is the residual phase obtained after n^{th} phase reconstruction iteration and $\tilde{\varphi}(\mathbf{r},n)$ is an approximation of the true phase function $\varphi(\mathbf{r})$ by a set of local $\{\tilde{\varphi}_l(\mathbf{r},n)\}$ and piston $\{\Delta_l^{(n)}\}$ phases obtained after n^{th} iteration. An ideal phase reconstruction corresponds to $\tilde{\varphi}(\mathbf{r}) = \varphi(\mathbf{r}) + const$ and yields to $St = 1$. The Strehl ratio value in Eq. (8) can also be associated with performance of an adaptive system referred to here as MAPR AO which uses conjugation of the sensor's output phase $\tilde{\varphi}_n(\mathbf{r})$ after each phase reconstruction iteration as adaptive optics wavefront control strategy.

3.3. Numerical analysis of phase reconstruction performance

Compare efficiency of phase reconstruction with MAPR and lens-analyzer sensors using an identical set of computer generated input field realizations described in section 3.1. This efficiency can be evaluated by considering dependences of the averaged Strehl ratios $\langle St(n)\rangle$ on the number of the phase reconstruction iterations n. As seen from the corresponding averaged Strehl ratio curves $\langle St(n)\rangle$ in Fig. 8, reconstruction of phase in the MAPR sensor occurs significantly faster than in the lens analyzer.

4. CONCLUSION

We introduced and analyzed the performance of a new wavefront sensor referred to as multi-aperture phase reconstruction (MAPR) sensor. This sensor is specifically developed for simultaneous high-resolution sensing of optical field wavefront phase under conditions of strong intensity scintillations. This sensor merges the Shack-Hartmann and the phase diversity wavefront sensing paradigms by integrating both zonal (aperture division) and modal (phase retrieval over entire aperture) approaches. The input wavefront is sub-divided into equally-sized zones defined by low-resolution lenslet sub-apertures. In each zone high-resolution phase retrieval is based on an iterative processing of the corresponding subsets of the pupil- and focal-plane intensity distributions that are similar to the phase diversity wavefront sensing technique. The final step of phase reconstruction over the entire aperture includes retrieval of piston phases based on minimization of the introduced continuity metric. It is shown that due to the parallel nature of the optical and signal processing, the MAPR sensor can provide significantly faster phase reconstruction and can operate robustly even in conditions of strong intensity scintillation.

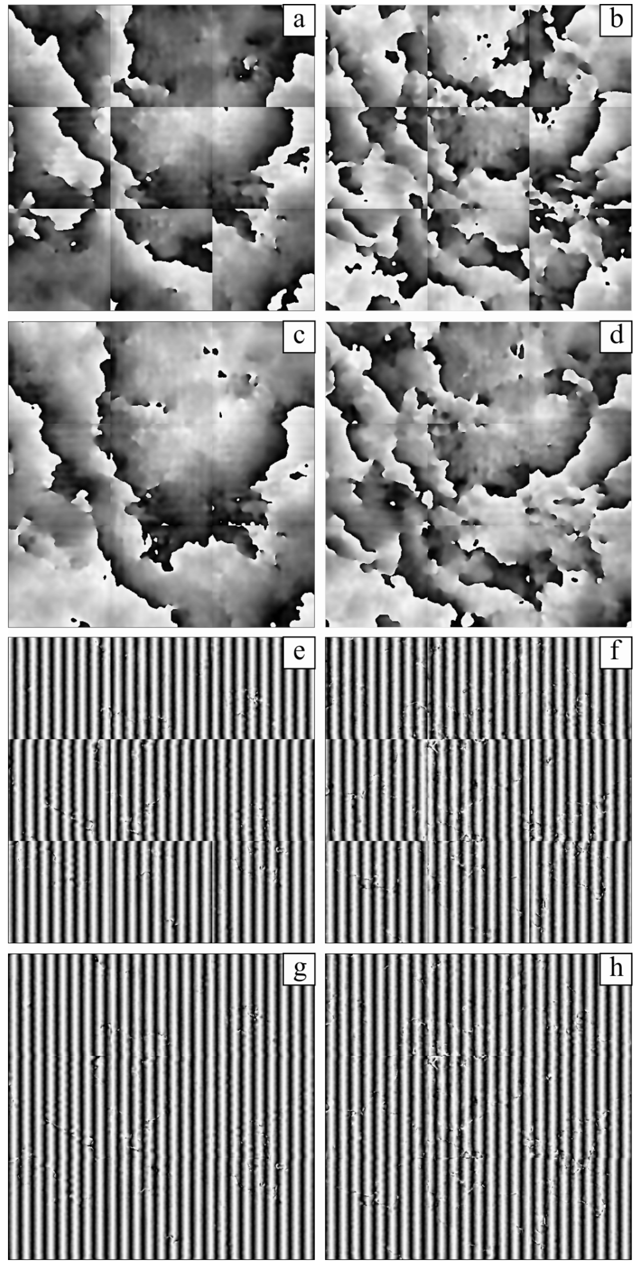

Fig. 7: Phase distributions (a-d) and the corresponding interference patterns (e-h) obtained after $n = 200$ phase reconstruction iterations using the pupil- and focal-plane intensity distributions from Figs. 4(a,b) and 6(a,b). The phase distributions are shown before (a,b) and after (c,d) piston phase recovery. The corresponding interferograms of the residual phase $\varphi(\mathbf{r}) - \tilde{\varphi}(\mathbf{r})$ are shown in (e-h): before (e,f) and after (g,h) piston phase computation.

ACKNOWLEDGEMENTS

The authors want to thank Svetlana Lachinova for the helpful discussions.

REFERENCES

[1] Zavorotnyi, V., U., "Strong fluctuations of the wave intensity behind a randomly inhomogeneous layer," Radiophys. Quantum Electron. 22, 352-354 (1979).

[2] Rytov, M., C., Kravtsov, Y., A. and Tatarskii, V., I., [Principles of Statistical Radiophysics 4 Wave Propagation Through Random Media], Springer-Verlag (1989).

[3] Andrews, L., C., Phillips, R., L., Hopen, C., Y. and Al-Habash, M.. A., "Theory of optical scintillation," J. Opt. Soc. Am. 16 (1999).

[4] Hardy, J., W., [Adaptive Optics for Astronomical Telescopes], Oxford U. Press (1998).

[5] Barchers, J., D., Fried, D., L. and Link, D., J., "Evaluation of the performance of Hartmann sensors in strong scintillation," Appl. Opt. 41, 1012-1021 (2002).

[6] Roddier, F., "Curvature sensing and compensation: a new concept in adaptive optics," Appl. Opt. 27, 1223-1225 (1988).

[7] Rousset, G., "Wavefront sensors," in [Adaptive Optics in Astronomy], Roddier, F., Cambridge U. Press, New York, pp. 91-130 (1999).

[8] Hardy, J., W., Lefebvre, J., E. and Koliopoulos, C., L., "Real-time atmospheric compensation," J. Opt. Soc. A. 67, 360-369 (1977).

[9] Sandler, D., G., Cuellar, L., Lefebvre, M., Barrett, T., Arnold, R., Johnson, P., Rego, A., Smith, G., Taylor, B. and Spiv, G., “Shearing interferometry for laser-guide-star atmospheric correction at large D/r0,” J. Opt. Soc. Am. A 11, 858-873 (1994).
[10] Gerchberg, R.. W. and Saxton, W., O., “A practical algorithm for the determination of phase from image and diffraction plane pictures,” Optik 35, 237-246 (1972).
[11] Gonsalves, R., A., “Phase retrieval from modulus data,” J. Opt. Soc. Am. 66, 961-964 (1976).
[12] Ivanov, V., Yu., Sivokon, V., P. and Vorontsov, M., A., “Phase retrieval from a set of intensity measurements: theory and experiment,” J. Opt. Soc. Am. A 9, 1515-1524 (1992).
[13] Paxman, R., G. and Fienup, J., R., “Optical misalignment sensing and image reconstruction using phase diversity,” J. Opt. Soc. Am. A 5, 914-923 (1988).
[14] Fienup, J., R., “Phase retrieval algorithms: a comparison,” Appl. Opt. 21, 2758-2769 (1982).
[15] Fienup, J., R. and Wackerman, C., C., “Phase-retrieval stagnation problems and solutions,” J. Opt. Soc. Am. A 3, 1897-1907 (1986).
[16] Fried, D., L., "Branch point problem in adaptive optics," J. Opt. Soc. Am. A 15, 2759-2768 (1998).
[17] Fried, D., L. and Vaughn, J., L., "Branch cuts in the phase function," Appl. Opt. 31, 2865-2882 (1992).

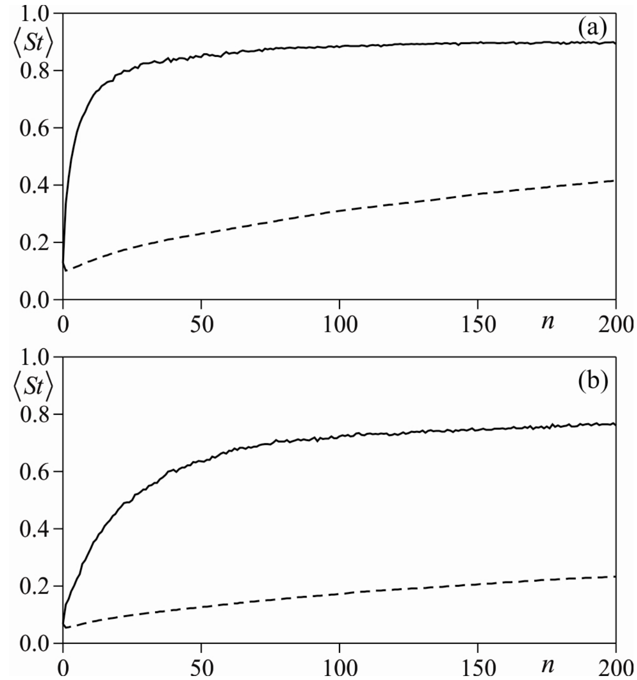

Fig. 8: Phase reconstruction convergence process in the MAPR wavefront sensor with 3×3 lenslet array (solid lines) and in the lens analyzer sensor (dashed lines) for $D/r_0 = 8$ (a), and $D/r_0 = 12$ (b).

[18] Vorontsov, M., A. and Sivokon, V., P., "Stochastic parallel-gradient-descent technique for high-resolution wave-front phase-distortion correction," J. Opt. Soc. Am. A 15, 2745-2758 (1998).
[19] Fleck, J., A., Morris, J., R. and Feit, M., D., “Time dependent propagation of high energy laser beam through the atmosphere,” Appl. Phys. 11, 329-335 (1977).
[20] Roggemann, M., C. and Welsh, B., [Imaging Through Turbulence], CRC Press (1996).
[21] Fried, D., L., "Anisoplanatism in adaptive optics," J. Opt. Soc. Am. 72, 52-61 (1982).
[22] Justh, E., W., Vorontsov, M., A., Carhart, G., W., Beresnev, L., A. and Krishnaprasad, P., S., "Adaptive optics with advanced phase-contrast techniques. II. High-resolution wave-front control," J. Opt. Soc. Am. A 18, 1300-1311 (2001).